



Benefits of global earth observation missions for disaggregation of exposure data and earthquake loss modeling: evidence from Santiago de Chile

Christian Geiß¹ · Peter Priesmeier² · Patrick Aravena Pelizari¹ · Angélica Rocío Soto Calderon³ · Elisabeth Schoepfer¹ · Torsten Riedlinger¹ · Mabé Villar Vega⁴ · Hernán Santa María^{5,6} · Juan Camilo Gómez Zapata^{7,8} · Massimiliano Pittore^{7,9} · Emily So¹⁰ · Alexander Fekete² · Hannes Taubenböck¹

Received: 24 March 2022 / Accepted: 8 October 2022
© The Author(s) 2022

Abstract

Exposure is an essential component of risk models and describes elements that are endangered by a hazard and susceptible to damage. The associated vulnerability characterizes the likelihood of experiencing damage (which can translate into losses) at a certain level of hazard intensity. Frequently, the compilation of exposure information is the costliest component (in terms of time and labor) of risk assessment procedures. Existing models often describe exposure in an aggregated manner, e.g., by relying on statistical/census data for given administrative entities. Nowadays, earth observation techniques allow the collection of spatially continuous information for large geographic areas while enabling a high geometric and temporal resolution. Consequently, we exploit measurements from the earth observation missions TanDEM-X and Sentinel-2, which collect data on a global scale, to characterize the built environment in terms of constituting morphologic properties, namely built-up density and height. Subsequently, we use this information to constrain existing exposure data in a spatial disaggregation approach. Thereby, we establish dasymmetric methods for disaggregation. The results are presented for the city of Santiago de Chile, which is prone to natural hazards such as earthquakes. We present loss estimations due to seismic ground shaking and corresponding sensitivity as a function of the resolution properties of the exposure data used in the model. The experimental results underline the benefits of deploying modern earth observation technologies for refined exposure mapping and related earthquake loss estimation with enhanced accuracy properties.

Keywords Exposure modeling · Disaggregation techniques · Earth observation · Remote sensing · Seismic risk · Earthquake loss estimation

✉ Christian Geiß
christian.geiss@dlr.de

Extended author information available on the last page of the article

1 Introduction

Earthquakes represent a devastating natural hazard that caused more than 1.7 million documented fatalities in the past 100 years globally (Wyss and Speiser 2022). Prospectively, the ongoing continuous increase of the world population (UN 2019) can be expected to put more people at risk in both rural (Wyss 2018) and urban environments (Bilham 2009; Wyss et al. 2021), respectively, than ever before. For the development of mitigation strategies for these perils, detailed knowledge about affiliated risks is in demand. As an important constituent element of natural hazard risk, the exposure and vulnerability need to be determined (UNISDR 2009). In particular, it is crucial to have detailed information about the spatiotemporal distribution of population as well as about the properties of the building inventory with respect to an expected level of seismic ground shaking. Especially for loss estimation, the collection of highly resolved building inventory information normally represents the most time-consuming and expensive aspect. Traditional data collection procedures foresaw detailed in situ building-by-building analysis by, e.g., structural engineers and small-scale population surveying (e.g., Dunbar et al. 2003; Kechidi et al. 2021). This may provide very detailed and high-quality information. However, such time-demanding and cost-intensive approaches are decreasingly able to cope with the high spatiotemporal dynamics of built environments. Simultaneously, the information provided on a coarser spatial level, such as spatially aggregated census data (e.g., Corbane et al. 2017; Santa Maria et al. 2017; Yepes-Estrada et al. 2017), hampers the consideration of small-scale hazard effects in a downstream risk model (Gomez Zapata et al. 2021; Nievas et al. 2022) and frequently shows a high level of uncertainty (Pittore et al. 2017). Moreover, recent empirical works underlined that the accuracy of damage estimates is very sensitive regarding the exposure component (Gomez-Zapata et al. 2022a, b), whereby the coarsest aggregation levels were found to be the most inaccurate (Senouci 2018; Dabbeek et al. 2021).

Recent assessment approaches already identified earth observation (EO) data as a valuable source of information for exposure estimation (Geiß and Taubenböck 2013). This is especially true for the latest generation optical sensors which enable the detection and characterization of objects of built environments within hazard-prone areas (e.g., Ehrlich and Tenerelli 2013; Geiß et al. 2017a). Related studies aimed at an integrative view on vulnerability and considered numerous parameters for a holistic assessment (e.g., Taubenböck et al. 2008; Ebert et al. 2009). Therefore, the derivation of a wide variety of vulnerability-related parameters from remote sensing, comprising population characteristics (e.g., Dobson et al. 2000; Aubrecht et al. 2013) and properties of the built environment (e.g., Mueller et al. 2006; French and Muthukumar 2006; Sahar et al. 2010), was explored. Given the nature of remote sensing as a tool for providing physical measurements of the earth's surface, the physical vulnerability of built environments, in particular, has been subject to increasing scientific contemplation over the course of the last decade. Numerous approaches were postulated for seismic vulnerability assessment: Sarabandi and Kiremidjian (2007) estimate the structural type of buildings based on remote sensing and ancillary tax assessor information for deployment in earthquake loss estimation models. Taubenböck et al. (2009), Borzi et al. (2011), Polli and Dell'Acqua (2011), and Qi et al. (2017) characterize the built environment with remote sensing data and retrieve specific fragility functions or damage probability matrices, respectively. In contrast to that, e.g., Borfecchia et al. (2010), Geiß et al. (2015a, 2017b, 2018; 2014), Liuzzi et al. (2019), Liu et al. (2019), Torres et al. (2019), and An et al. (2021) combined limited in situ ground truth information characterizing

the building inventory with features from remote sensing and use techniques of statistical inference for a complete labeling of the residual building inventory according to specific vulnerability levels or more generic properties such as construction material or occupancy, respectively. Related methodological principles were also exploited by, e.g., Wieland et al. (2012, 2016), Pittore and Wieland (2013), Geiß et al. (2016), Pittore et al. (2020), and Fan et al. (2021) to assess seismic vulnerability or related parameters on a coarser spatial level to allow for the use of data with larger spatial coverage. Recently, Aravena Pelizari et al. (2021) deployed street-level imagery that was extracted from the GoogleStreetView platform and classified various seismic structural types with deep learning models to automatically compile relevant in situ data.

At the same time, data requirements for exposure modeling still hamper utilization capabilities for large areas of many approaches. This is due to data availability, monetary costs of data, and processing demand of, e.g., very high spatial resolution EO imagery and detailed in situ data. Moreover, local idiosyncrasies must not be bypassed and transfer of models cannot be carried out in a non-adaptive manner since, e.g., building structural types may feature a large variability of morphological appearance and vulnerability in different parts of the world. As a consequence, population data and building inventory information with affiliated vulnerability characteristics are frequently still outdated, spatially discontinuous, or aggregated. Thus, affiliated natural hazard risk assessment strategies do not provide a picture of risk on large scales such as nations, continents, or the entire globe, while enabling a high spatial, thematic, and temporal resolution.

In parallel, with the advent of the big earth data epoch, novel data collection mechanisms have become available on a global scale. The latest generation EO missions, which are highly relevant for characterization of built environments, such as ESA/EU's Copernicus Sentinel-2 mission (Drusch et al. 2012) and German Aerospace Center's spaceborne radar interferometer TanDEM-X (TDM) (Krieger et al. 2007), collect planetary data with unprecedented spatial and temporal resolution properties. In particular, the Sentinel-2 satellites provide multispectral imagery with 10-m spatial resolution and high temporal coverage (i.e., 10 days at the equator with one satellite, and 5 days with 2 satellites; 2–3 days at mid-latitudes), whereas, the TDM provides a digital surface model with 12-m spatial resolution.

Consequently, in this paper, we capitalize upon this globally existing EO data to derive constituent morphologic properties of the built environment, i.e., *built-up density* and *height*. Subsequently, we develop dasymetric disaggregation techniques to spatially allocate and eventually constrain existing exposure data from administrative entities based on the derived morphologic properties of the built environment. Finally, we align vulnerability information, i.e., fragility functions, to the exposure data and establish probabilistic seismic hazard analysis-based (PSHA) seismic loss estimations for the earthquake-prone city of Santiago de Chile. Thereby, we evaluate the loss estimation accuracies as a function of the resolution properties of the underlying exposure data. This is done to gain insights regarding how the different aggregation levels of the exposure data propagate into final loss estimates.

The remainder of the paper is organized as follows. We provide a brief description of the study site and incorporated datasets in Sect. 2. Section 3 documents the developed and implemented methods for hazard assessment, disaggregation of exposure data, and loss estimation, whereas Sect. 4 contains affiliated results and discussion. Conclusions and future perspectives are outlined in Sect. 5.

2 Study site and data

2.1 Santiago de Chile

We apply the proposed methods to data that cover Santiago de Chile, the capital of Chile. The corresponding metropolitan area is inhabited by more than 7 million people and is located in close proximity to the subduction zone where the Nazca Plate subducts the South American Plate. However, the seismic hazard for Santiago de Chile is not only determined by the offshore subduction zone, but also by shallow crust earthquakes. These events emanate from inland faults on the western flank of the Andean Cordillera, i.e., the Western Andean Thrust (Ammirati et al. 2019). Among them is also the recently characterized San Ramon Fault. This active North–South oriented west verging fault system runs directly along the eastern border of the city (Armijo et al. 2010) and represents a likely source for damaging events (Hussain et al. 2020).

2.2 Data

2.2.1 National exposure model for Chile

We built upon the national exposure model for Chile which was developed in the context of the South America Risk Assessment (SARA) project (available online: <https://sara.openquake.org/risk:exposure>) (GEM 2014; Yepes-Estrada et al. 2017). The exposure data were predominately generated from census data in combination with planning permission data and comprises the spatial distribution, number, and living area of residential structures, which are classified according to 18 seismic building structural types with associated replacement costs. The information is provided on three spatial levels, i.e., *comuna* (corresponding to urban districts or municipalities), provinces, and regions. For this work, we deploy the *comuna*-level data (Fig. 1a). Thereby, the planning permission data can be considered as the most reliable data source and were compiled on *comuna* level. Consequently, we utilize this level since it provides the most favorable tradeoff between spatial resolution and reliability (Santa Maria et al. 2017; Yepes-Estrada et al. 2017).

Additionally, we integrate population information for subsequent casualty estimates from the national exposure model for Chile. The population information for the *comuna* level was compiled from national population statistics. In particular, the data reveals the average number of dwellers per building type at the legal place of residency, i.e., the nighttime population (Yepes-Estrada et al. 2017).

2.2.2 Earth observation data for characterization of the built environment

To derive *built-up density* and *height*, we follow an automated workflow. First, “built-up” and “non-built-up” areas are distinguished by integrating the so-called Global Urban Footprint layer (Esch et al. 2017). We integrate this information in a tailored filtering procedure for the TDM digital surface model (DSM) data (Geiß et al. 2015b) to extract elevation information for built-up areas, i.e., a normalized DSM (nDSM) (Geiß et al. 2020a) for Santiago de Chile (Fig. 1b). Subsequently, the intra-urban land cover is mapped under consideration of multispectral Sentinel-2 imagery. Thereby, intra-urban

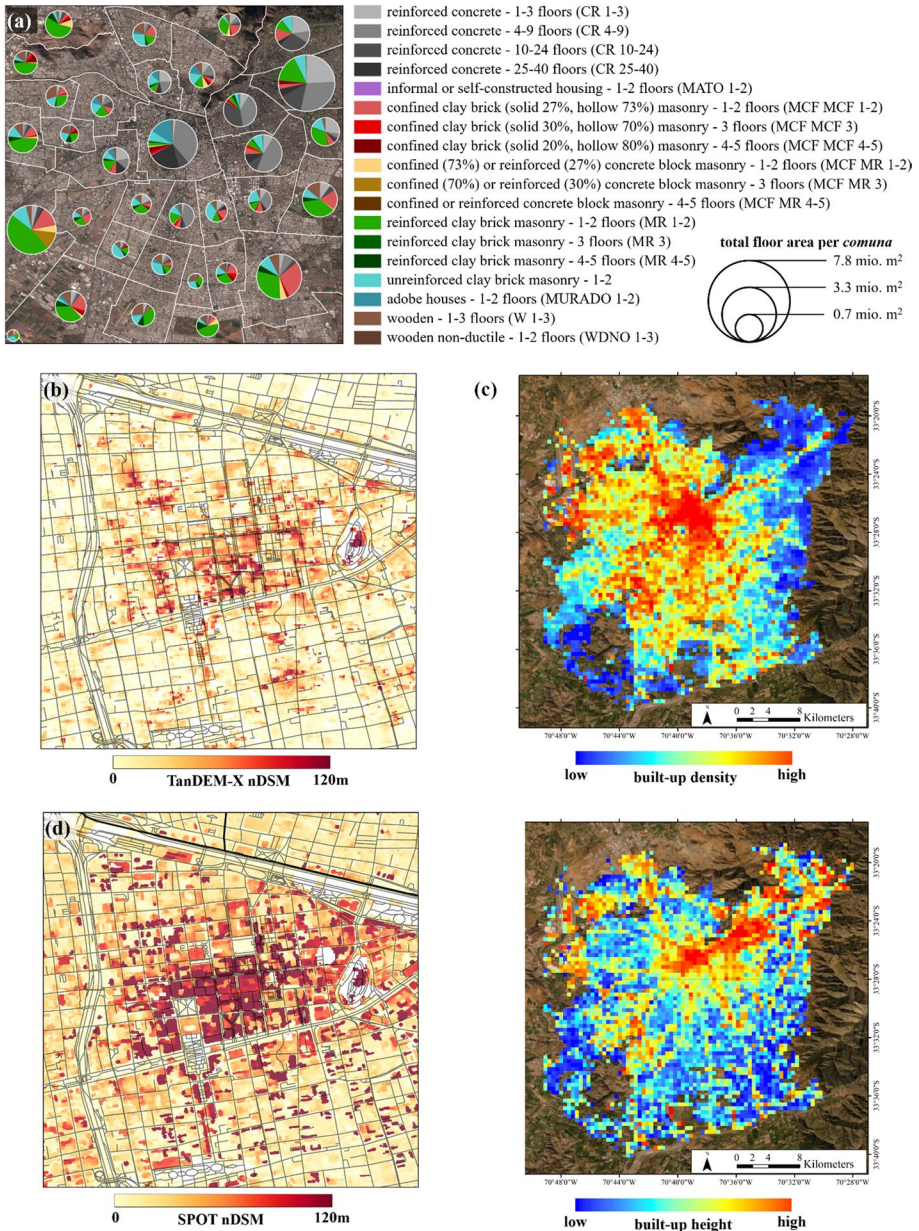


Fig. 1 Input data for the exposure mapping workflow; **a** administrative entities on *comuna* level of the national exposure model for Chile with corresponding shares of 18 different seismic building structural types for Santiago de Chile; **b** visualization of the normalized digital surface model (nDSM) derived from the TanDEM-X DSM which contains heights of objects which are elevated from the earth's surface such as buildings or vegetation; **c** built-up density (upper map) and height (lower map) estimation based on the TanDEM-X nDSM data and additional Sentinel-2 imagery for Santiago de Chile on grid-cell level; color coding from low to high corresponds to equally-spaced quantiles and visualizes, thus, the relative distribution of built-up density and height values, respectively; **d** visualization of the SPOT nDSM with very high spatial resolution used for validation purposes

vegetation is pruned and the residual elevated areas, i.e., elevated built-up areas, serve as the basis to compute *built-up densities* and *heights*. These two measures were combined for a morphologic characterization of the built environment for spatial entities, i.e., rectangular grid cells, with a side length of 500 m (Fig. 1c) (Geiß et al. 2019). It is here where it can be noted that those grid-cell-level estimates can be also produced by means of supervised learning techniques, i.e., learning from an area where both TDM and Sentinel-2 are available and establishing an estimation for areas where solely Sentinel-2 is available. Despite existing globally, the TDM DSM is frequently solely accessible for up to 100 000 km² for scientific applications (Geiß et al. 2019), whereas the Sentinel-2 imagery is accessible without any restrictions. A suite of corresponding techniques was recently proposed in Geiß et al. (2022a, b; 2020b).

Finally, we obtained a very high resolution (VHR) DSM for validation purposes, which was derived from panchromatic tri-stereo images with a geometric resolution of 2 m acquired by the SPOT-7 satellite (d'Angelo et al. 2008). From it, also an nDSM was derived (Fig. 1d).

2.2.3 Fragility functions for earthquake loss estimation and empirical conversion factors for casualty estimation

Subsequently, we align vulnerability information, i.e., existing analytical fragility functions (Villar-Vega et al. 2017), to the seismic structural types contained in the exposure model for Santiago de Chile. The fragility functions establish the likelihood of damage conditional on a certain level of ground shaking, i.e., earthquake intensity. We mainly rely on functions that were specifically developed for the South American building inventory and local regional dataset of strong ground motion records. The structural capacity of each building class was computed from 150 single-degree-of-freedom oscillators which enable the propagation of building-to-building variabilities. In addition, the seismic demand was considered by over 300 ground motion records to account for record-to-record variabilities. The structural capacity for each building class was determined based on several existing studies, outcomes from two workshops organized in South America, and expert judgment by multiple local practitioners (GEM 2014). Thereby, ductility levels, damage schemes, and response behaviors were considered. Finally, each fragility function was modeled as a cumulative lognormal distribution, and the representative intensity measures (PGA, SA—0.3 s, SA—1.0 s) were selected based on the correlation between ground shaking and damage distribution. Four damage states are discriminated, i.e., “slight,” “moderate,” “extensive,” and “destroyed” (Villar-Vega et al. 2017). The set of fragility functions was completed by integrating functions from HAZUS (FEMA 2015) for the types MCF MCF 4–5, MCF MR 4–5, and MR 4–5, respectively. The fragility functions were harmonized and aligned to the structural types of Santiago de Chile as documented in detail in Fig. 2.

To anticipate the possible effects of damaging earthquakes on the exposed population, we further integrate empirical conversion factors for the building-related damage states for casualty estimation. We built upon conversion factors from HAZUS (FEMA 2015). Thereby, four degrees of injury are distinguished, which are all caused by direct consequences of an earthquake such as collapsing buildings, and falling debris (Spence and So 2021). The degrees of injury comprise: “slightly injured,” “moderately injured,” “heavily injured,” and “deadly injured.” The degrees of injury are aligned to the damage states as documented in detail in Table 1. It can be noted that the damage state “destroyed” was further distinguished according to “destroyed—with collapse” and “destroyed—without

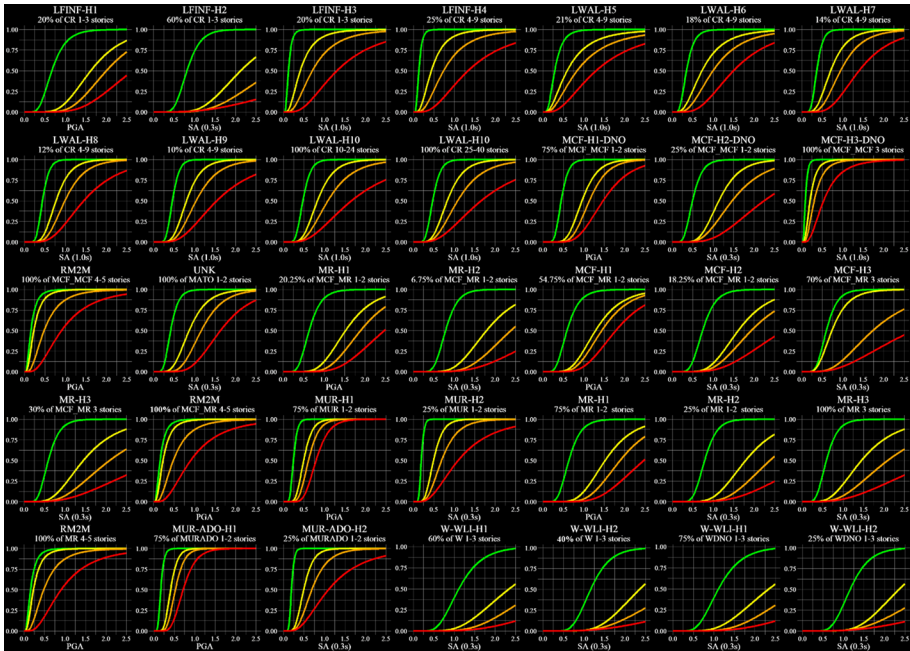


Fig. 2 Deployed fragility functions which establish a relationship between the intensity of an earthquake (x-axis) and corresponding degree of damage (y-axis) for four damage states, i.e., green=“slight,” yellow=“moderate,” orange=“extensive,” and red=“destroyed,” respectively, for the seismic building structural types of Santiago de Chile

collapse.” The latter describes cases where a structure faces substantial damage which prevents repairing it. However, without a collapse, the number of deadly injured inhabitants will be substantially reduced compared to a structure that faces the damage pattern “destroyed—with collapse.”

3 Implemented methods

A flowchart of the implemented methods is given in Fig. 3. First, we carry out PSHA with four probabilities of occurrence for Santiago de Chile (Sect. 3.1). Section 3.2 details the developed dasymmetric disaggregation techniques to spatially disaggregate and eventually constrain the existing exposure data from the national model on *comuna* level. Finally, Sect. 3.3 contains the description of implemented damage state computation and casualty estimation procedures.

3.1 Probabilistic seismic hazard assessment

For the characterization of the seismic hazard, we capitalize upon the SARA seismic hazard model according to Garcia et al. (2017), which follows the well-known PSHA approach (Cornell 1968). The input data for the model encompasses a database of seismically active faults, as well as seismological, geological, and geophysical information. Additionally, focal

Table 1 Conversion factors for casualty estimation (%) as a function of structural type and damage state

Structural type	Damage state																			
	Slight				Moderate				Extensive				Destroyed—without collapse				Destroyed—with collapse			
	Slight	Moderate	Heavy	Dead	Slight	Moderate	Heavy	Dead	Slight	Moderate	Heavy	Dead	Slight	Moderate	Heavy	Dead	Slight	Moderate	Heavy	Dead
CR 1-3	0.05	0	0	0	0.25	0.03	0	0	1	0.1	0.001	0.001	5	1	0.01	0.01	40	20	5	10
CR 4-9	0.05	0	0	0	0.25	0.03	0	0	1	0.1	0.001	0.001	5	1	0.01	0.01	40	20	5	10
CR 10-24	0.05	0	0	0	0.25	0.03	0	0	1	0.1	0.001	0.001	5	1	0.01	0.01	40	20	5	10
CR 25-40	0.05	0	0	0	0.25	0.03	0	0	1	0.1	0.001	0.001	5	1	0.01	0.01	40	20	5	10
MATO 1-2	0.05	0	0	0	0.35	0.4	0.001	0.001	2	0.2	0.002	0.002	10	2	0.02	0.02	40	20	5	10
MCF MCF 1-2	0.05	0	0	0	0.2	0.025	0	0	1	0.1	0.001	0.001	5	1	0.01	0.01	40	20	5	10
MCF MCF 3	0.05	0	0	0	0.2	0.025	0	0	1	0.1	0.001	0.001	5	1	0.01	0.01	40	20	5	10
MCF MCF 4-5	0.05	0	0	0	0.2	0.025	0	0	1	0.1	0.001	0.001	5	1	0.01	0.01	40	20	5	10
MCF MR 1-2	0.05	0	0	0	0.2	0.025	0	0	1	0.1	0.001	0.001	5	1	0.01	0.01	40	20	5	10
MCF MR 3	0.05	0	0	0	0.2	0.025	0	0	1	0.1	0.001	0.001	5	1	0.01	0.01	40	20	5	10
MCF MR 4-5	0.05	0	0	0	0.2	0.025	0	0	1	0.1	0.001	0.001	5	1	0.01	0.01	40	20	5	10
MR 1-2	0.05	0	0	0	0.2	0.025	0	0	1	0.1	0.001	0.001	5	1	0.01	0.01	40	20	5	10
MR 3	0.05	0	0	0	0.2	0.025	0	0	1	0.1	0.001	0.001	5	1	0.01	0.01	40	20	5	10
MR 4-5	0.05	0	0	0	0.2	0.025	0	0	1	0.1	0.001	0.001	5	1	0.01	0.01	40	20	5	10
MUR1-2	0.05	0	0	0	0.35	0.4	0.001	0.001	2	0.2	0.002	0.002	5	1	0.01	0.01	40	20	5	10
MURADO 1-2	0.05	0	0	0	0.35	0.4	0.001	0.001	2	0.2	0.002	0.002	5	1	0.01	0.01	40	20	5	10
W 1-3	0.05	0	0	0	0.25	0.03	0	0	1	0.1	0.001	0.001	5	1	0.01	0.01	40	20	3	5
WDNO 1-3	0.05	0	0	0	0.25	0.03	0	0	1	0.1	0.001	0.001	5	1	0.01	0.01	40	20	3	5

The numerical values represent percentage shares of the population per building. In subsequent estimations, differences in casualties per structural type occur, since the different structural types have a varying probability to reach a certain damage state

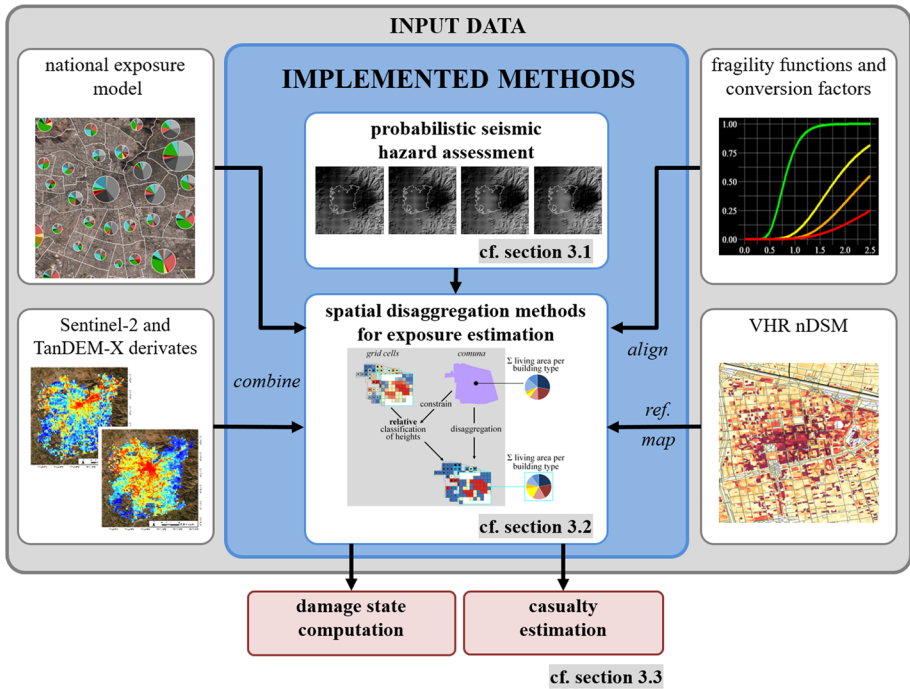


Fig. 3 Overview of the implemented methods for hazard characterization, exposure modeling, damage state computation, and casualty estimation, respectively

mechanisms for the Nazca subduction zones are integrated along with a harmonized earthquake catalog for South America, and a selection of ground motion prediction equations (GMPEs). These input data allow for modeling of the near-surface seismic properties in South America, the subduction zones, and the processes within the continental plate. (i) The shallow seismicity is approximated by both an integrated model of distributed seismicity and crustal fault sources; (ii) the subduction interface seismicity is modeled as large 3D fault sources geometry; (iii) the subduction in-slab seismicity is considered via 3D volumes of ruptures describing the spatial location of events within the area of interest (Garcia et al. 2017). Modeling results, in combination with the GMPEs (the epistemic uncertainty is accounted for by using a Logic Tree-based procedure), allow for a probabilistic determination of the expected earthquake intensity. For the actual seismic hazard computations for Santiago de Chile we used the OpenQuake Engine (Pagani et al. 2014). The model reveals peak ground acceleration (PGA) and spectral acceleration (SA—0.3 s, SA—1.0 s). We consider four probabilities of occurrence to analyze a broad spectrum of events, i.e., earthquakes with a probability of occurrence of 50%, 30%, and 10% within 50 years, and an extreme event with 10% in 475 years, respectively. Lastly, we spatially refine the modeled intensity values with an exact interpolation technique, i.e., inverse distance weighting (Shepard 1968), to obtain an intensity value every 300 m (Fig. 4).

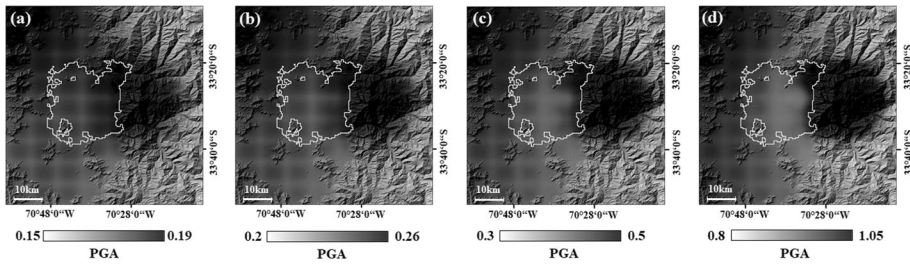


Fig. 4 PGA with a probability of occurrence of **a** 50%, **b** 30%, and **c** 10% within 50 years, and **d** an extreme event with 10% in 475 years. The white contour line represents the settlement area under study of Santiago de Chile

3.2 Spatial disaggregation methods for exposure estimation

Generally, disaggregation methods establish a mapping that foresees transforming data from one set of coarse spatial units (i.e., source zone) to one set of finer spatial units (i.e., target zone) (Wu et al. 2005). We used for all disaggregation approaches exposure data from the *comuna* level as source zone and deployed EO-based datasets as target zone.

As an initial means, we implemented a linear disaggregation approach with respect to the settlement area. Thereby, the living areas per building type on *comuna* level are disaggregated proportionally regarding the settlement area on grid-cell level (Fig. 5). Consequently, the linear disaggregation corresponds to a so-called binary dasymmetric mapping approach, since the redistribution of the living areas per building type is solely established according to the binary expression of a variable (i.e., presence or absence of “built-up areas”). In our application context, such a disaggregation scheme is, in particular, helpful to establish a more differentiated consideration of the hazard intensity, since each grid cell will be assigned an individual hazard intensity value instead of solely considering one hazard intensity value per *comuna*.

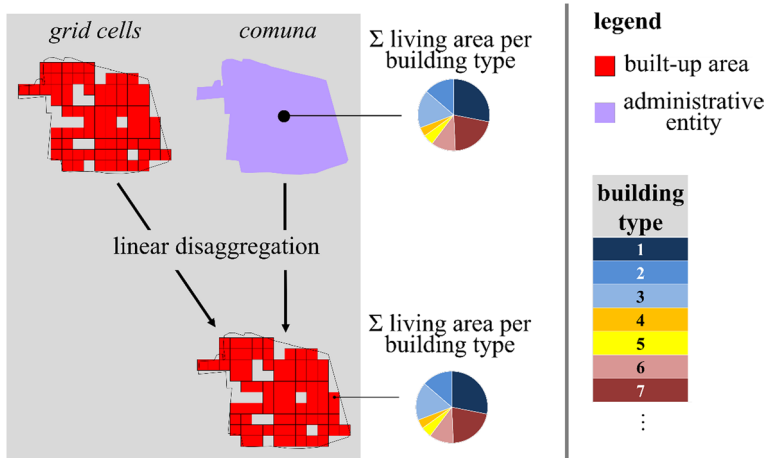


Fig. 5 Linear disaggregation approach for exposure estimation. The living areas per building type (pie chart) on *comuna* level are disaggregated proportionally regarding the settlement area on grid-cell level

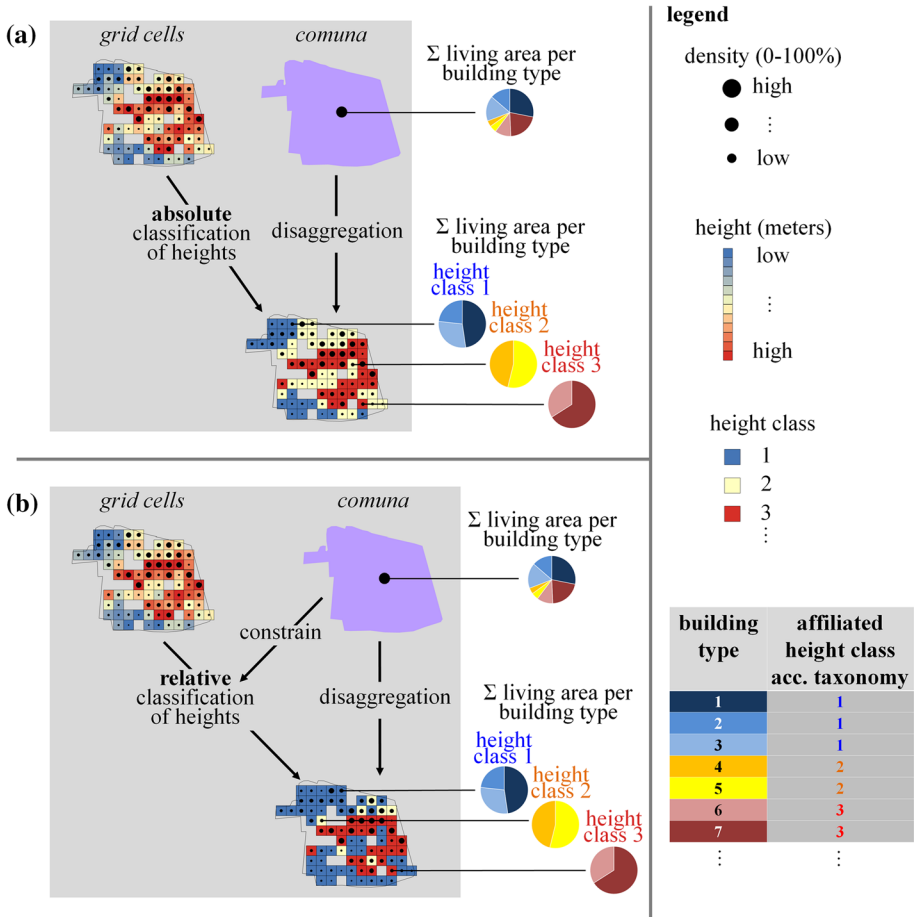


Fig. 6 Disaggregation methods for exposure estimation which take the urban morphology into account: disaggregation approaches on grid-cell level with **a** absolute and **b** relative height constraints

However, to establish a more differentiated mapping, we incorporate the derived morphologic properties of the built environment for disaggregation. Figure 6 illustrates the dasymetric disaggregation approaches on grid-cell level with both absolute and relative height constraints.

First, the EO-based *built-up height* measurements are classified into up to six distinct building height classes as defined by the height classes of the building structural types. Here, the classification according to absolute height thresholds (Fig. 6a) follows the number of floors of the respective height classes (Table 2), whereby we apply a value of three meters per floor. In contrast, the classification according to relative height thresholds (Fig. 6b) reproduces the distribution of the height classes on *comuna* level exactly. Generally, the classifications determine which structural types can occur in a certain grid cell (i.e., one up to nine types per cell) (Table 2).

Table 2 Seismic building structural types with affiliated height class

Height class	1–2 floors	3 floors	4–5 floors	6–9 floors	10–24 floors	25–40 floors
Building structural type	MR-1–2, MCF MCF-1–2, MUR-1–2, W-1–3, CR-1–3, MCF MR-1–2, MURADO-1–2, WDNO-1–2, MATO-1–2	MCF MCF-3, MR-3, MCF MR-3	MR-4–5, MCF MCF-4–5, MCF MR-4–5	CR-4–9	CR-10–24	CR-25–40

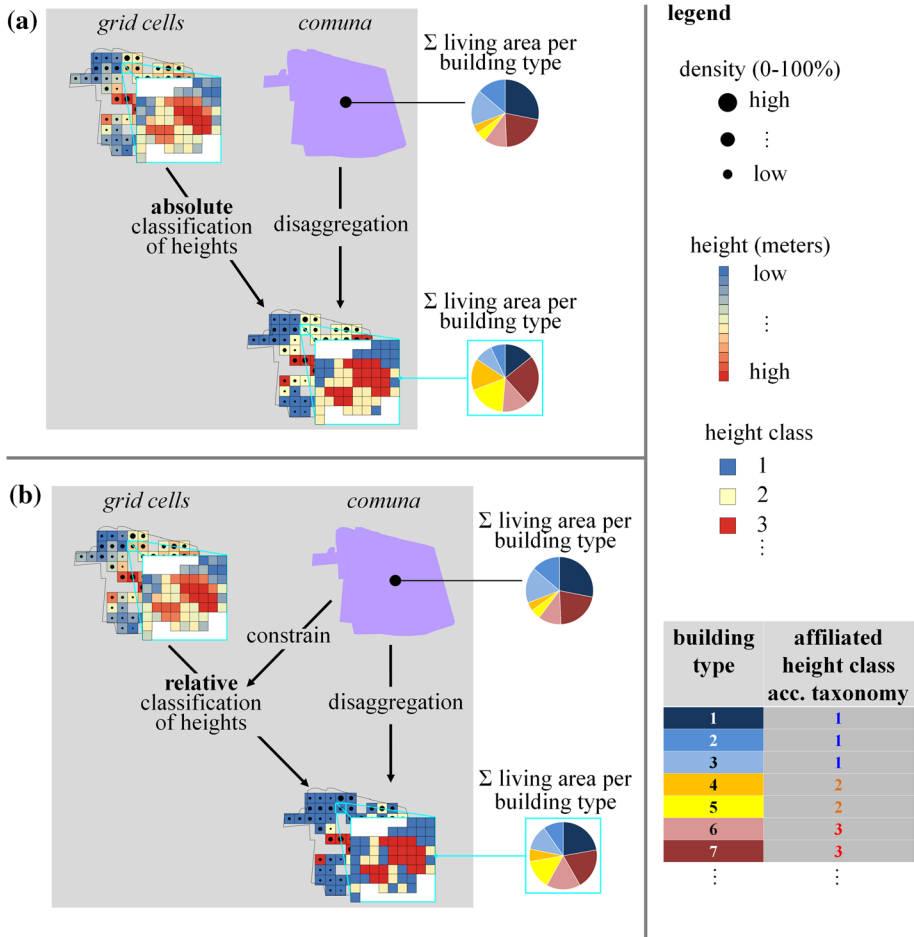


Fig. 7 Disaggregation methods for exposure estimation which take the urban morphology into account: disaggregation approaches on sub-grid-cell level with **a** absolute and **b** relative height constraints

Additionally, the living areas per building height class are summed up on *comuna* level. The sum per specific building height class is redistributed over the grid cells which correspond to that specific building height class while preserving the characteristic shares of individual structural types of that specific building height class. Finally, the *built-up density* is deployed to disaggregate the living areas in a weighted manner, i.e., the living areas per building height class are redistributed proportionally regarding the corresponding *built-up densities*. For subsequent usage, we divide the mapped living area per building type by corresponding average living areas per building type (according to the numbers included in the national exposure model) to obtain the absolute number of buildings per type.

Figure 7 illustrates the disaggregation approaches on sub-grid-cell level. We follow the same aforementioned methodological principles. However, here we deploy the TanDEM-X

Fig. 8 **a** Results of the different mapping techniques regarding the number of buildings per type. Color bars for individual building types correspond to absolute number of buildings per grid cell (or area equivalent for each *comuna*). **b** Results of the different mapping techniques regarding the number of buildings per type. Color bars for individual building types correspond to absolute number of buildings per grid cell (or area equivalent for each *comuna*)

nDSM values of the elevated built-up areas, i.e., elevated intra-urban areas, whereby vegetation has been pruned, in order to consider all eventually existing building height classes within a grid cell. Consequently, the absolute and relative classification reveals a distribution of the different building height classes on grid-cell level. In detail, the classification according to absolute height thresholds (Fig. 7a) follows the number of stories per building height class (Table 2). Analogous to the grid-cell-level approach, the classification according to relative height thresholds (Fig. 7b) reproduces the distribution of the building height classes on *comuna* level exactly.

In addition to that, for subsequent casualty estimation, the mapped number of buildings per type is also deployed to compute the population per building, since the *comuna*-level data also carries the average number of dwellers per building type.

3.3 Damage state computation and casualty estimation

To assess the likely distribution of damage levels on the exposed building portfolio after the occurrence of an earthquake, the estimated ground shaking intensity is assigned to each spatial entity. Given the spatial resolution properties of the hazard assessment with an intensity value every 300 m, it is possible that multiple intensity values are located within a spatial entity of an exposure model. If this is the case, we compute the mean intensity value per spatial entity. Consequently, we can determine the intensity which affects a certain number of buildings of a certain type at a certain location. In conjunction with the type-specific fragility functions, the overall distribution of damage states for a spatial entity can be computed. Population data per building and affiliated damage states are combined with the empirical conversion factors for the building-related damage states. Finally, the numbers across the buildings are summed up to obtain the number of affected people according to the four degrees of injury per spatial entity.

4 Experimental results and discussion

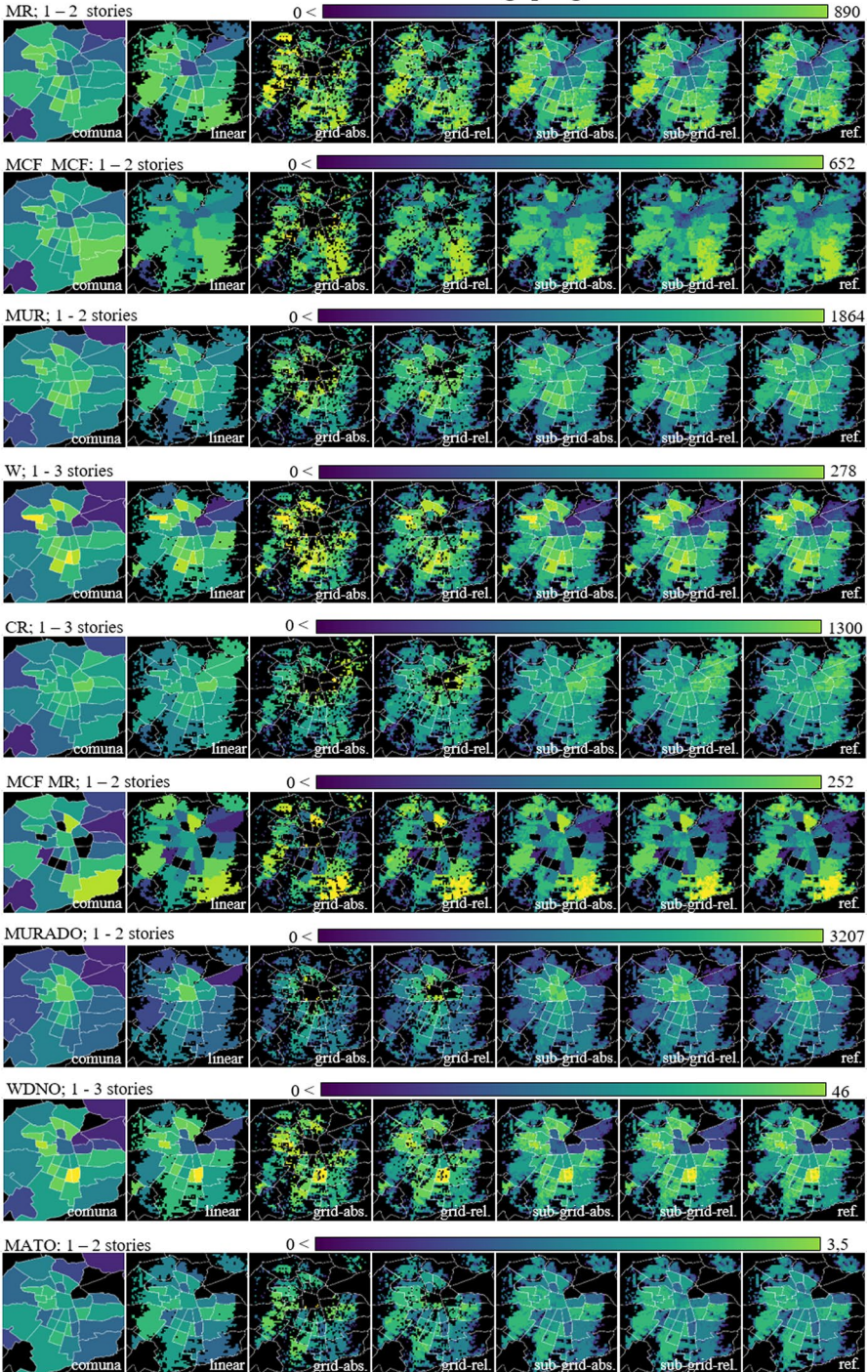
4.1 Exposure data

The results of the five different disaggregation techniques along with the *comuna*-level data regarding the number of buildings per type are visualized in Fig. 8a, b. Additionally, to establish a reference mapping, we deploy the VHR nDSM (which can be considered as a proper measurement) on sub-grid-cell level while reproducing the building height class distributions on *comuna* level, since this configuration corresponds to the highest level of prior knowledge deployment. Moreover, the building types are ordered according to their frequency, i.e., “MR 1–2” corresponds to the most frequent type in Santiago de Chile, whereas “CR 25–40” represents the least frequent type.

From these figures, it can be first noted that distributions of buildings per type within a *comuna* are less uniform for the grid-cell-level methods compared to the sub-grid-cell

building type

number of buildings per grid cell



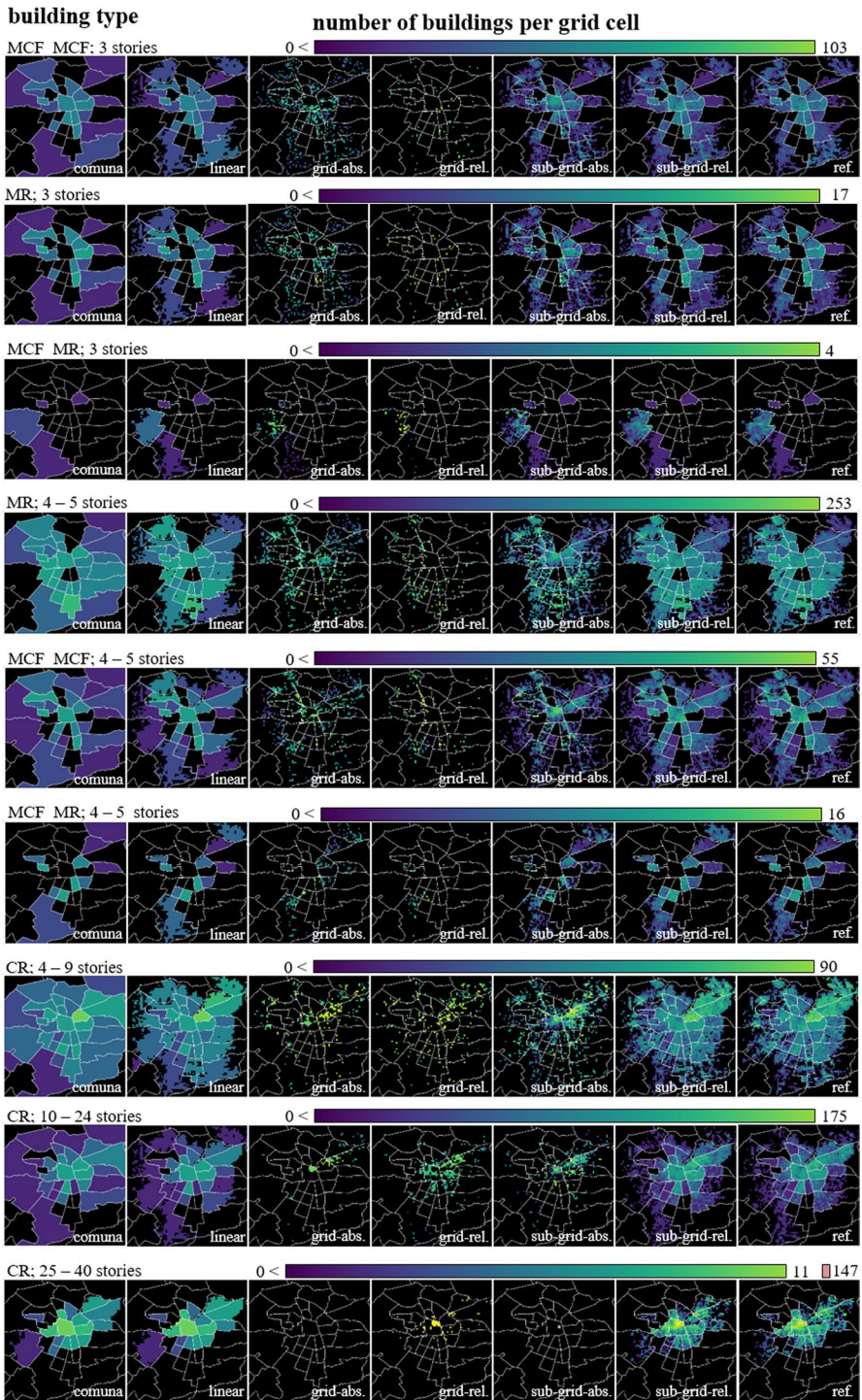


Fig. 8 (continued)

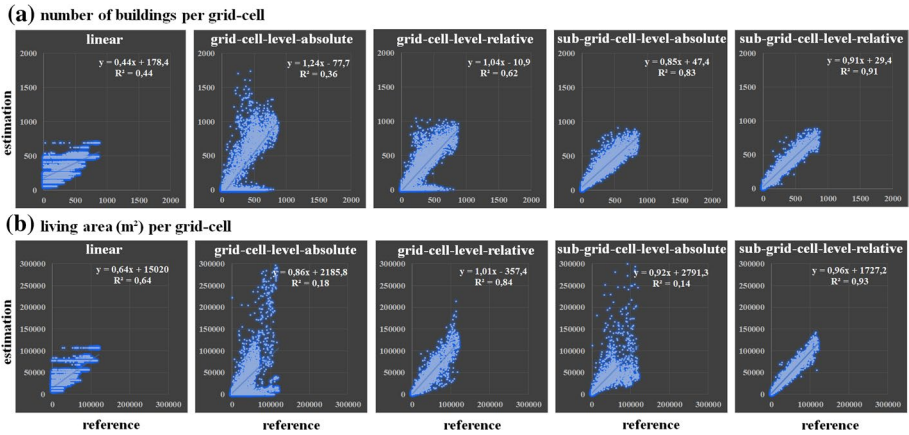


Fig. 9 Scatter plots for estimated **a** number of buildings and **b** corresponding living area (m^2) for the different disaggregation techniques, i.e., linear, grid-cell-level-absolute, grid-cell-level-relative, sub-grid-cell-level-absolute, and sub-grid-cell-level-relative, respectively

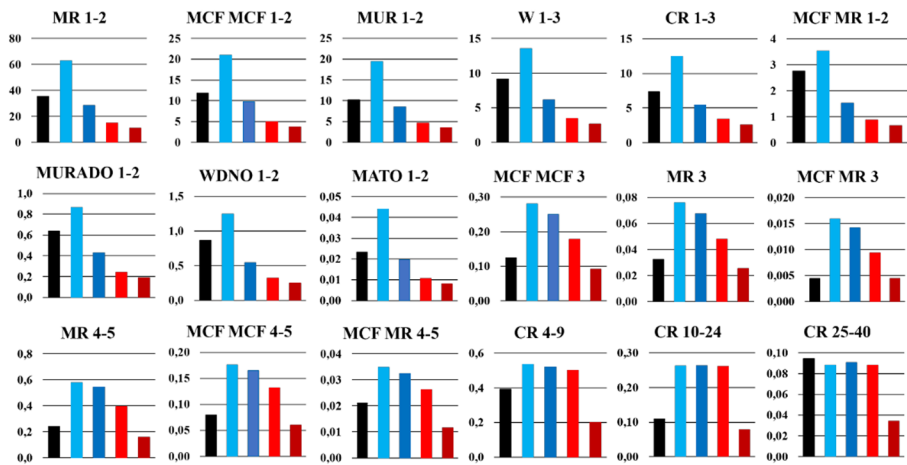
methods. This is intrinsically related to the fact that solely a single building height class per grid cell can be inferred on grid-cell level for disaggregation. However, also the estimates at the sub-grid-level allocate the different building types to specific parts of the *comunas*. These mappings reflect the reference spatial distributions frequently very well. This underlines the importance of spatially refined mappings compared to linear disaggregations, which solely provide uniform estimates within a *comuna*.

To study the accuracy properties of the different disaggregation methods in detail in this empirical setup, scatter plots (Fig. 9) provide a comparison per grid cell for both the number of buildings and the living area (since it varies per building type). Notably, grid-cell-level and sub-grid-cell-level estimates, which are based on relative height constraints, allow obtaining consistently moderate to high positive levels of agreement ($R > 0.6$) for both the number of buildings and living area. These estimates are substantially better aligned than linear allocations. In contrast, the methods that build upon absolute height thresholds are hardly capable of reproducing the reference mapping. This stresses the necessity to extract proper distributions of building height classes from the initial exposure model since those can hardly be estimated directly with the presented data and without further prior knowledge.

As mentioned in Sect. 2.2.2, the grid-cell-level estimates can be also produced by means of supervised learning techniques, i.e., learning from an area where both TDM and Sentinel-2 are available and establishing an estimation for areas where solely Sentinel-2 is available. Consequently, the accuracy difference of the grid-cell level and sub-grid-cell level can be interpreted as an error cost related to the integration of both TDM DSM data and Sentinel-2 imagery compared to the ubiquitously available Sentinel-2 imagery.

Additionally, Fig. 10 provides median absolute errors (MAEs) both in terms of the number of buildings per grid cell and living area (m^2) per grid cell for the different building types. Analogous to previous observations, the grid-cell-level estimates based on absolute height thresholds (light blue) do not provide superior accuracy properties compared to linear allocations (black). In contrast, both grid-cell-level-relative (dark blue) and sub-grid-cell-level-absolute (light red) estimates provide substantial benefits for buildings of the lowest building height class (which corresponds to the vast majority of buildings in this empirical setting, i.e., 99.0% of the number and 68.6% of the living area). Moreover, the

(a) median absolute error – number of buildings per grid-cell



(b) median absolute error – living area (m²) per grid-cell

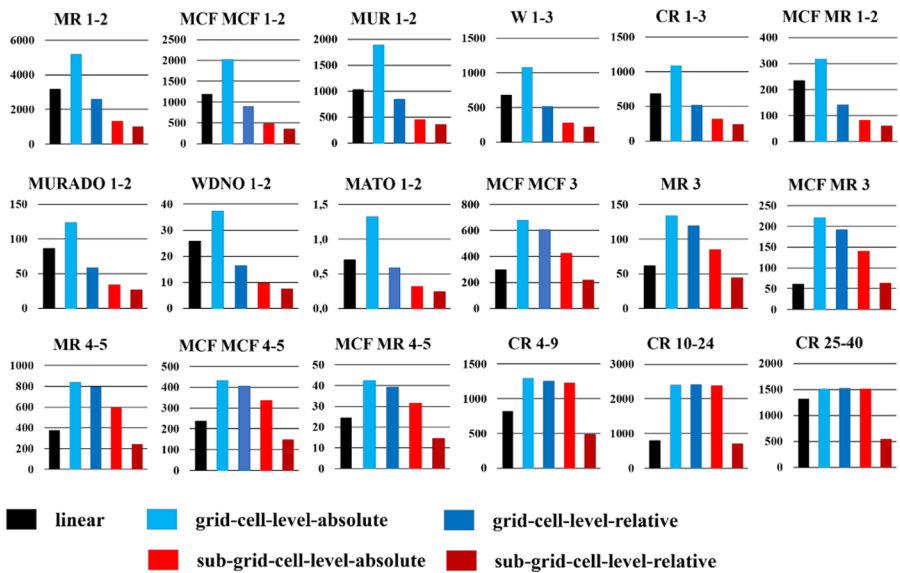


Fig. 10 Median absolute errors for **a** the number of buildings per grid-cell and **b** the living area (m²) per grid-cell regarding the different disaggregation techniques and seismic building structural types, respectively

sub-grid-cell-level-relative approach (dark red) allows the establishment of more accurate estimates for each building type compared to a linear disaggregation which unambiguously underlines the usefulness of the presented data and methods.

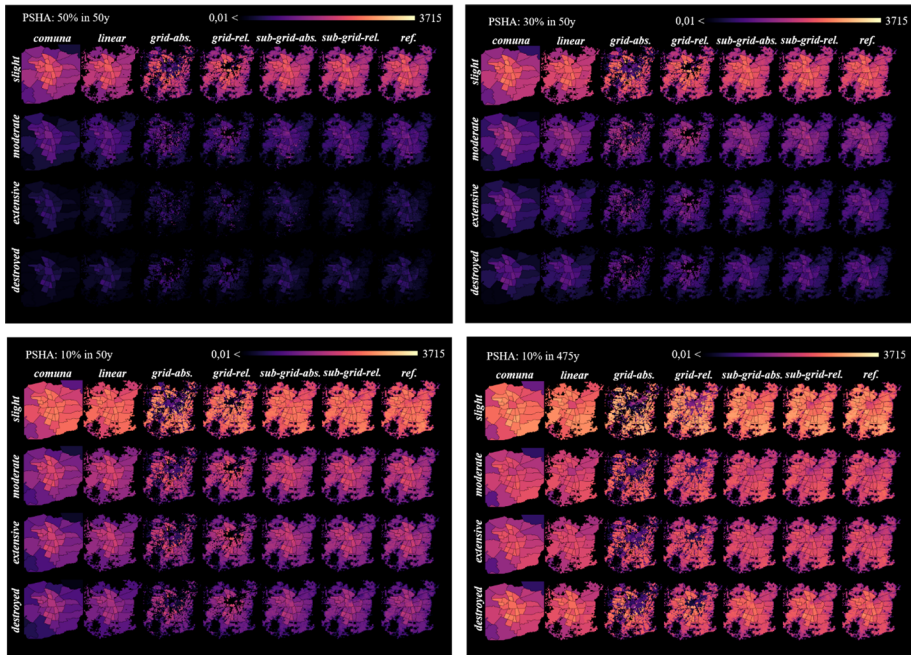


Fig. 11 Results of the different mapping techniques regarding the four damage states and PSHA results. The color bars indicate the absolute number of buildings per grid cell according to a certain damage state and PSHA result, respectively

4.2 Damage state computation and casualty estimation

Figure 11 provides the damage states for the spatial entities according to the four considered PSHA results. It can be visually traced how the number of damaged buildings increases with increasing intensity of shaking. Thereby, large parts of the business and financial areas, which expand northeastwards from the city center, feature a comparatively low concentration of damaged buildings. This is more pronounced for the grid-cell-level approaches compared to the sub-grid-cell-level approaches due to a denser spatial pooling of high-rise buildings (cf. Fig. 8b). Generally, the underlying mechanism relates to the existence of high-rise buildings in the city center, which are typically compliant with seismic design provisions and thus, having low fragility. In contrast, particularly for the considered severe events, i.e., earthquakes with a probability of occurrence of 10% within 50 years and with 10% in 475 years, respectively, we observe that large areas at the fringes of the city might feature a high concentration of damaged buildings, which relates to the existence of numerous low-rise building types with a comparative higher seismic fragility (e.g., informal, non-engineered structures). Overall, different damage is estimated for different parts of the city, which allow for anticipation of the situation based on possible events.

Figure 12 shows MAEs, which describe the deviation regarding the estimated number of buildings per grid cell in relation to the reference number of buildings per grid cell, for the four damage states and PSHA results. Thus, MAEs indicate the numerical deviation that relates to the majority of grid cells, i.e., area. Except for the grid-cell-level-absolute

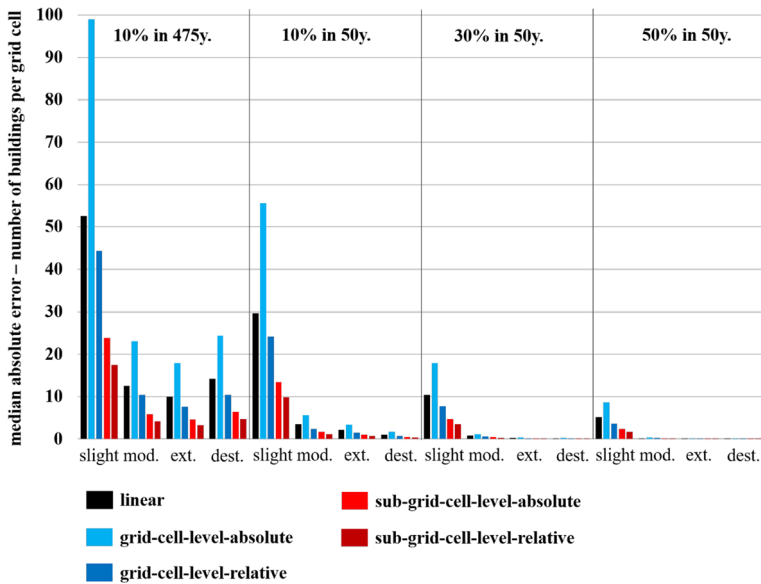


Fig. 12 Median absolute errors regarding the number of buildings per grid cell for the four damage states and PSHA results

approach, the proposed disaggregation techniques all provide substantial benefits in terms of their accuracy properties compared to linear disaggregation which confirms the benefits of the presented data and methods. Thereby, the sub-grid-cell-level approaches are more favorable than the grid-cell-level-relative method, whereby the relative height constraints on the sub-grid-cell level reveal the most favorable results overall.

Finally, Figs. 13 and 14 provide the percentages of the population in the respective casualty state for the spatial entities according to the four PSHA results and the corresponding MAEs of the different disaggregation techniques, respectively. Analogous to the disaggregated damage state mappings, large parts of the center and areas in the Northeast feature a comparatively low concentration of people in the respective casualty states. In contrast, various areas arranged in a concentric manner around the core of the city represent particular hot spots for casualties. Thereby, sub-grid-level-relative estimates provide superior MAEs. The casualty estimates can serve as a metric for prioritizing rescue activities and further mitigation efforts after an earthquake.

5 Conclusion and outlook

In this paper, we established a workflow for the derivation of constituent morphologic properties of the built environment and subsequent utilization for spatial disaggregation of exposure information based on globally existing EO data, i.e., TDM DSM data and Sentinel-2 imagery. Hereby, we proposed five different disaggregation techniques to allocate various seismic building structural types. Moreover, we aligned building fragility functions and conversion factors for casualty estimation and utilized the compiled data for

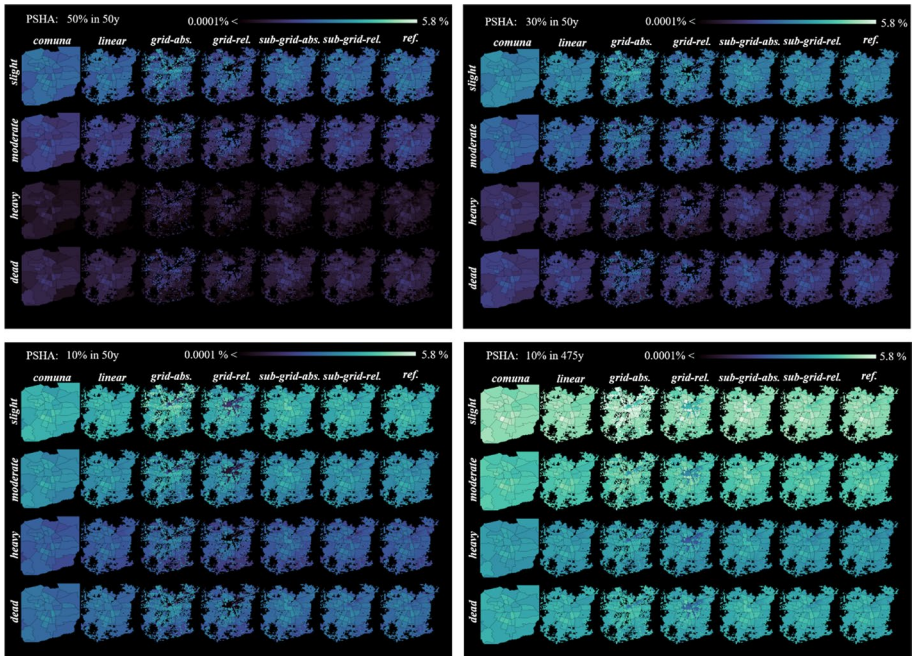


Fig. 13 Results of the different mapping techniques regarding the four damage states and PSHA results. The color bars indicate the percentage of the population in the respective casualty state

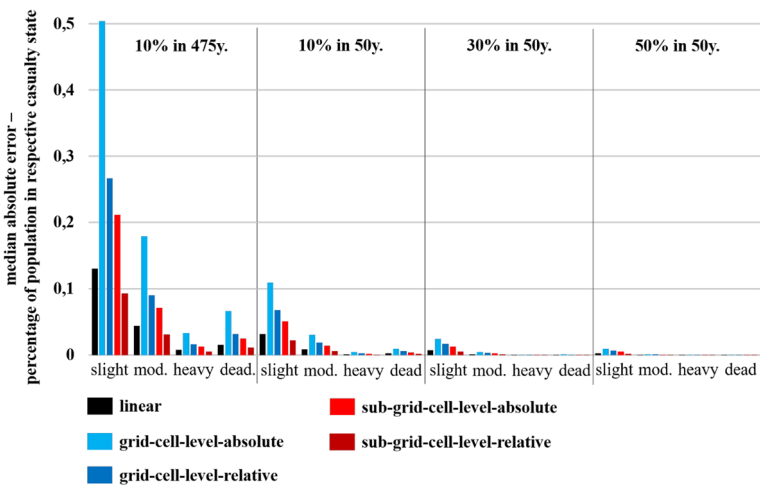


Fig. 14 Median absolute errors regarding the percentage of the population in the respective casualty state and PSHA results

PSHA-based earthquake loss estimations. The proposed disaggregation methods turned out to be beneficial for a fine-grained mapping of various seismic building structural types and refined estimates of both building damage and casualties. Based on our estimates of

damage and casualties, resulting from a variety of accelerations, one may formulate an informed mitigation program.

In the future, we aim to integrate machine learning techniques (Geiß et al. 2020b, 2022a, b) in the workflow to overcome restrictions related to the accessibility of the TDM DSM data and apply the workflow on a country scale for Chile. Thereby, it can be expected that the relevance of the proposed disaggregation techniques will be increased given that some *comunas* particularly in rural areas expand over comparatively small settlement areas, i.e., solely a minor fraction of the area of a *comuna* is covered by settlements, and, thus, fail to allow for a spatially differentiated consideration of small-scale hazard effects. Consequently, with a refined exposure mapping, we aim to better quantitatively describe risks from various earthquakes, especially in rural areas.

Funding Open Access funding enabled and organized by Projekt DEAL. The work of Christian Geiß was supported by the Helmholtz Association under the grant “pre_DICT” (PD-305). This study has been conducted as part of the projects RIESGOS (Grant No. 03G0876A-D) and RIESGOS 2.0 (03G0905A-B), funded by the German Federal Ministry of Education and Research (BMBF). The authors have no relevant financial or non-financial interests to disclose. All authors contributed to the study conception and design. Majority of material preparation, data collection and analysis were performed by Christian Geiß, Peter Priesmeier, Patrick Aravena Pelizari, and Angélica Rocio Soto Calderon. The first draft of the manuscript was written by Christian Geiß and Peter Priesmeier and all authors commented on previous versions of the manuscript. All authors read and approved the final manuscript.

Declarations

Conflict of interest The authors have not disclosed any competing interests.

Open Access This article is licensed under a Creative Commons Attribution 4.0 International License, which permits use, sharing, adaptation, distribution and reproduction in any medium or format, as long as you give appropriate credit to the original author(s) and the source, provide a link to the Creative Commons licence, and indicate if changes were made. The images or other third party material in this article are included in the article’s Creative Commons licence, unless indicated otherwise in a credit line to the material. If material is not included in the article’s Creative Commons licence and your intended use is not permitted by statutory regulation or exceeds the permitted use, you will need to obtain permission directly from the copyright holder. To view a copy of this licence, visit <http://creativecommons.org/licenses/by/4.0/>.

References

- Ammirati JB, Vargas G, Rebolledo S, Abrahami R, Potin B, Leyton F, Ruiz S (2019) The crustal seismicity of the western andean thrust (Central Chile, 33°–34° S): implications for regional tectonics and seismic hazard in the Santiago Area. *Bull Seismol Soc Am* 109(5):1985–1999. <https://doi.org/10.1785/0120190082>
- An J, Nie G, Hu B (2021) Area-Wide estimation of seismic building structural types in rural areas by using decision tree and local knowledge in combination. *Int J Disaster Risk Reduct* 60:102320. <https://doi.org/10.1016/j.ijdr.2021.102320>
- Aravena Pelizari P, Geiß C, Aguirre P, Santa Maria H, Merino Peña Y, Taubenböck H (2021) Automated building characterization for seismic risk assessment using street-level imagery and deep learning. *ISPRS J Photogramm Remote Sens* 180:370–386
- Armijo R, Rauld R, Thiele R, Vargas G, Campos J, Lacassin R, Kausel E (2010) The West Andean thrust, the San Ramon fault, and the seismic hazard for Santiago, Chile. *Tectonics* 29:TC2007. <https://doi.org/10.1029/2008TC002427>
- Aubrecht C, Özceylan D, Steinocher K, Freire S (2013) Multi-level geospatial modeling of human exposure patterns and vulnerability indicators. *Nat Hazards* 68:147–163. <https://doi.org/10.1007/s11069-012-0389-9>

- Bilham RG (2009) The seismic future of cities. *Bull Earthq Eng* 7:839–887. <https://doi.org/10.1007/s10518-009-9147-0>
- Borfecchia F, Pollino M, De Cecco L, Lugari A, Martini S, La Porta L, Ristatore E, Pascale C (2010) Active and passive remote sensing for supporting the evaluation of the urban seismic vulnerability. *Italian J Remote Sens* 42(3):129–141
- Borzi B, Dell'Acqua F, Faravelli M, Gamba P, Lisini G, Onida M, Polli D (2011) Vulnerability study on a large industrial area using satellite remotely sensed images. *Bull Earthq Eng* 9:675–690. <https://doi.org/10.1007/s10518-010-9211-9>
- Corbane C, Hancilar U, Ehrlich D, Dr Groeve T (2017) Pan-European seismic risk assessment: a proof of concept using the Earthquake Loss Estimation Routine (ELER). *Bull Earthq Eng* 15(3):1057–1083. <https://doi.org/10.1007/s10518-016-9993-5>
- Cornell C (1968) Engineering seismic risk analysis. *Bull Seismol Soc Am* 58(5):1583–1606. <https://doi.org/10.1785/BSSA0580051583>
- d'Angelo P, Lehner M, Krauss T, Hoja D, Reinartz P (2008) Towards automated DEM generation from high resolution stereo satellite images. *The International Archives of the Photogrammetry, Remote Sensing and Spatial Information Sciences*, XXXVII (B4)
- Dabbeek J, Crowley H, Silva V, Weatherill G, Paul N, Nievas CI (2021) Impact of exposure spatial resolution on seismic loss estimates in regional portfolios. *Bull Earthq Eng*. 19:5819-5841. <https://doi.org/10.1007/s10518-021-01194-x>
- Dobson JE, Bright EA, Coleman PR, Durfee RC, Worley BA (2000) LandScan: a global population database for estimating populations at risk. *Photogramm Eng Remote Sens* 66(7):849–857
- Drusch M, Del Bello U, Carlier S, Colin O, Fernandez V, Gascon F, Hoersch B, Isola C, Laberinti P, Martimort P, Meygret A, Spoto F, Sy O, Marchese F, Bargellini P (2012) Sentinel-2: ESA's optical high-resolution mission for GMES operational services. *Remote Sens Environ* 120:25–36. <https://doi.org/10.1016/j.rse.2011.11.026>
- Dunbar PK, Bilham RG, Laituri MJ (2003) Earthquake loss estimation for india based on macroeconomic indicators. *Risk Sci Sustain* 112:163–180. https://doi.org/10.1007/978-94-010-0167-0_13
- Ebert A, Kerle N, Stein A (2009) Urban social vulnerability assessment with physical proxies and spatial metrics derived from air- and spaceborne imagery and GIS data. *Nat Hazards* 48:275–294. <https://doi.org/10.1007/s11069-008-9264-0>
- Ehrlich D, Tenerelli P (2013) Optical satellite imagery for quantifying spatio-temporal dimension of physical exposure in disaster risk assessments. *Nat Hazards* 68:1271–1289. <https://doi.org/10.1007/s11069-012-0372-5>
- Esch T, Heldens W, Hirner A, Keil M, Marconcini M, Roth A, Zeidler J, Dech S, Strano E (2017) Breaking new ground in human settlements from space—the Global Urban Footprint. *ISPRS J Photogramm Remote Sens* 134:30–42. <https://doi.org/10.1016/j.isprsjprs.2017.10.012>
- Fan X, Nie G, Xia C, Zhou J (2021) Estimation of pixel-level seismic vulnerability of the building environment based on mid-resolution optical remote sensing images. *Int J Appl Earth Obs Geoinf* 101(161–175):102339. <https://doi.org/10.1016/j.jag.2021.102339>
- FEMA (2015) Hazus—MH 2.1. Multi hazard loss estimation methodology: technical manual. earthquake model. Department of Homeland Security; Federal Emergency Management Agency; Mitigation Division. Washington D.C.
- French SP, Muthukumar S (2006) Advanced technologies for earthquake risk inventories. *J Earthq Eng* 10(2):207–236. <https://doi.org/10.1080/13632460609350594>
- Garcia J, Weatherill G, Pagani M, Rodriguez L, Poggi V (2017) Building an open seismic hazard model for South America: The SARA PSHA Model. SARA Hazard Working Group. In: 16th world conference on earthquake engineering, pp 1–13
- Geiß C, Taubenböck H (2013) Remote sensing contributing to assess earthquake risk: from a literature review towards a roadmap. *Nat Hazards* 68:7–48. <https://doi.org/10.1007/s11069-012-0322-2>
- Geiß C, Taubenböck H, Tyagunov S, Tisch A, Post J, Lakes T (2014) Assessment of seismic building vulnerability from space. *Earthq Spectra* 30(4):1553–1583. <https://doi.org/10.1193/121812EQS350M>
- Geiß C, Aravena Pelizari P, Marconcini M, Sengara W, Edwards M, Lakes T, Taubenböck H (2015a) Estimation of seismic buildings structural types using multi-sensor remote sensing and machine learning techniques. *ISPRS J Photogramm Remote Sens* 104:175–188. <https://doi.org/10.1016/j.isprsjprs.2014.07.016>
- Geiß C, Wurm M, Breunig M, Felbier A, Taubenböck H (2015b) Normalization of TanDEM-X DSM data in urban environments with morphological filters. *IEEE Trans Geosci Remote Sens* 53(8):4348–4362. <https://doi.org/10.1109/TGRS.2015.2396195>


- Geiß C, Gilge M, Lakes T, Taubenböck H (2016) Estimation of seismic vulnerability levels of urban structures with multisensor remote sensing. *IEEE J Sel Top Appl Earth Observ Remote Sens* 9(5):1913–1936. <https://doi.org/10.1109/JSTARS.2015.2442584>
- Geiß C, Schauß A, Riedlinger T, Dech S, Zelaya C, Guzmán N, Hube MA, Arsanjani JJ, Taubenböck H (2017a) Joint use of remote sensing data and volunteered geographic information for exposure estimation: evidence from Valparaíso. *Chile Natl Hazards* 86(1):81–105. <https://doi.org/10.1007/s11069-016-2663-8>
- Geiß C, Thoma M, Pittore M, Wieland M, Dech S, Taubenböck H (2017b) Multitask active learning for characterization of built environments with multisensor earth observation data. *IEEE J Sel Top Appl Earth Observ Remote Sens* 10(12):5583–5597. <https://doi.org/10.1109/JSTARS.2017.2748339>
- Geiß C, Thoma M, Taubenböck H (2018) Cost-sensitive multitask active learning for characterization of urban environments with remote sensing. *IEEE Geosci Remote Sens Lett* 15(6):922–926. <https://doi.org/10.1109/LGRS.2018.2813436>
- Geiß C, Leichte T, Wurm M, Aravena Pelizari P, Standfuß I, Zhu XX, So E, Siedentop S, Esch T, Taubenböck H (2019) Large-area characterization of urban morphology: mapping built-up height and density with the TanDEM-X mission and Sentinel-2. *IEEE J Sel Top Appl Earth Observ Remote Sens* 12(8):2912–2927. <https://doi.org/10.1109/JSTARS.2019.2917755>
- Geiß C, Aravena Pelizari P, Bauer S, Schmitt A, Taubenböck H (2020a) Automatic training set compilation with multisource geodata for DTM generation from the TanDEM-X DSM. *IEEE Geosci Remote Sens Lett* 17(3):456–460. <https://doi.org/10.1109/LGRS.2019.2921600>
- Geiß C, Schrader H, Aravena Pelizari P, Taubenböck H (2020b) Multistrategy ensemble regression for mapping of built-up height and density with Sentinel-2 data. *ISPRS J Photogramm Remote Sens* 170:57–71. <https://doi.org/10.1016/j.isprsjprs.2020.10.004>
- Geiß C, Brzoska E, Aravena Pelizari P, Lautenbach S, Taubenböck H (2022a) Multi-target regressor chains with repetitive permutation scheme for characterization of built environments with remote sensing. *Int J Appl Earth Obs Geoinf* 106:102657. <https://doi.org/10.1016/j.jag.2021.102657>
- Geiß C, Rabuske A, Aravena Pelizari P, Bauer S, Taubenböck T (2022b) Selection of unlabeled source domains for domain adaptation in remote sensing. *Array* 15:100233. <https://doi.org/10.1016/j.array.2022.100233>
- GEM (2014) Report on the SARA exposure and vulnerability workshop in Medellín, Colombia (Report produced in the context of the GEM South America integrated Risk Assessment (SARA) project No. Version 1.0-May 2014)
- Gomez-Zapata JC, Brinckmann N, Harig S, Zafir R, Pittore M, Cotton F, Babeyko A (2021) Variable-resolution building exposure modelling for earthquake and Tsunami scenario-based risk assessment. An application case in Lima, Peru. *Natl Hazard Earth Syst Sci* 21:3599–3628. <https://doi.org/10.5194/nhess-21-3599-2021>
- Gomez-Zapata JC, Pittore M, Cotton F, Lilienkamp H, Shinde S, Aguirre P, Santa Maria H (2022a) Epistemic uncertainty of probabilistic building exposure compositions in scenario-based earthquake loss models. *Bull Earthq Eng* 20:2401–2438. <https://doi.org/10.1007/s10518-021-01312-9>
- Gomez-Zapata JC, Zafir R, Pittore M, Merino Y (2022b) Towards a sensitivity analysis in seismic risk with probabilistic building exposure models: an application in Valparaíso, Chile using ancillary open-source data and parametric ground motions. *ISPRS Int J Geo-Inf* 11(2):113. <https://doi.org/10.3390/ijgi11020113>
- Hussain E, Elliott JR, Silva V, Vilar-Vega M, Kane D (2020) Contrasting seismic risk for Santiago, Chile, from near-field and distant earthquake sources. *Nat Hazard* 20:1533–1555. <https://doi.org/10.5194/nhess-20-1533-2020>
- Kechidi S, Castro JM, Monteiro R, Marques M, Yelles K, Bourahla N, Hamdache M (2021) Development of exposure datasets for earthquake damage and risk modelling: the case study of northern Algeria. *Bull Earthq Eng*. 19:5253–5283. <https://doi.org/10.1007/s10518-021-01161-6>
- Krieger G, Moreira A, Fiedler H, Hajnsek I, Werner M, Younis M, Zink M (2007) TanDEM-X: a satellite formation for high-resolution SAR interferometry. *IEEE Trans Geosci Remote Sens* 45(11):3317–3341. <https://doi.org/10.1109/TGRS.2007.900693>
- Liu Y, Li Z, Wie B, Li X, Fu B (2019) Seismic vulnerability assessment at urban scale using data mining and GIScience technology: application to Urumqi (China). *Geomat Nat Haz Risk* 10(1):958–985. <https://doi.org/10.1080/19475705.2018.1524400>
- Liuzzi M, Aravena Pelizari P, Geiß C, Masi A, Tramutoli V, Taubenböck H (2019) A transferable remote sensing approach to classify building structural types for seismic risk analyses: the case of Val d'Agri area (Italy). *Bull Earthq Eng* 17(9):4825–4853. <https://doi.org/10.1007/s10518-019-00648-7>

- Mueller M, Segl K, Heiden U, Kaufmann H (2006) Potential of high-resolution satellite data in the context of vulnerability of buildings. *Nat Hazards* 38:247–258. <https://doi.org/10.1007/s11069-005-8637-x>
- Nievas CI, Pilz M, Prehn K, Schorlemmer, Weatherill G, Cotton F (2022) Calculating earthquake damage building by building: the case of the city of Cologne, Germany. *Bull Earthq Eng* 20:1519–1565. <https://doi.org/10.1007/s10518-021-01303-w>
- Pagani M, Monelli D, Weatherill G, Danciu L, Crowley H, Silva V, Henshaw P, Butler L, Nastasi M, Panzeri L, Simionato M, Vigano D (2014) OpenQuake engine: an open hazard (and risk) software for the global earthquake model. *Seismol Res Lett* 85(3):692–702. <https://doi.org/10.1785/0220130087>
- Pittore M, Wieland M (2013) Toward a rapid probabilistic seismic vulnerability assessment using satellite and ground-based remote sensing. *Nat Hazards* 68(1):115–145. <https://doi.org/10.1007/s11069-012-0475-z>
- Pittore M, Wieland M, Fleming K (2017) Perspectives on global dynamic exposure modelling for georisk assessment. *Nat Hazards* 86(1):7–30. <https://doi.org/10.1007/s11069-016-2437-3>
- Pittore M, Haas M, Silva V (2020) Variable resolution probabilistic modeling of residential exposure and vulnerability for risk applications. *Earthq Spectra* 36(S1):321–344. <https://doi.org/10.1177/8755293020951582>
- Polli D, Dell’Acqua F (2011) Fusion of optical and SAR data for seismic vulnerability mapping of buildings. In: Prasad S, Bruce LM, Chanussot J (eds) *Optical remote sensing: advances in signal processing and exploitation techniques*. Springer, Heidelberg, pp 329–341
- Qi W, Su G, Sun L, Yang F (2017) Wu Y (2017) “Internet+” approach to mapping exposure and seismic vulnerability of buildings in a context of rapid socioeconomic growth: a case study in Tangshan, China. *Nat Hazards* 86:107–S139. <https://doi.org/10.1007/s11069-016-2581-9>
- Sahar L, Muthukumar S, French P (2010) Using aerial imagery and GIS in automated building footprint extraction and shape recognition for earthquake risk assessment of urban inventories. *IEEE Trans Geosci Remote Sens* 48(9):3511–3520. <https://doi.org/10.1109/TGRS.2010.2047260>
- Santa Maria H, Hube MA, Rivera F, Yepes-Estrada C, Valcarcel JA (2017) Development of national and local exposure models of residential structures in Chile. *Nat Hazards* 86:55–79. <https://doi.org/10.1007/s11069-016-2518-3>
- Sarabandi P, Kiremidjian A (2007) Development of algorithms or building inventory compilation through remote sensing and statistical inferencing. The John A. Blume Earthquake Engineering Center, Department of Civil and Environmental Engineering, Stanford University, Stanford, CA, USA, Report No 158, p 419
- Senouci A, Bard PY, Beck E, Farsi MN, Cartier S (2018) Mapping seismic vulnerability at urban scale: discussion on relevant cartography representations and smoothing for urban planning purposes on the Oran case study. *Soil Dyn Earthq Eng* 115:545–563. <https://doi.org/10.1016/j.soildyn.2018.08.034>
- Shepard D (1968) A two-dimensional interpolation function for irregularly-spaced data. In: Blue RB, Rosenberg AM (ed) *Proceedings of the 1968 23rd ACM national conference*. ACM Press, New York, pp 517–524
- Spence R, So E (2021) *Why do buildings collapse in earthquakes?: Building for safety in seismic areas*. Wiley. ISBN: 978-1-119-61942-0
- Taubenböck H, Post J, Roth A, Zosseder K, Strunz G, Dech S (2008) A conceptual vulnerability and risk framework as outline to identify capabilities of remote sensing. *Nat Hazard* 8:409–420. <https://doi.org/10.5194/nhess-8-409-2008>
- Taubenböck H, Roth A, Dech S, Mehl H, Münich JC, Stempniewski L, Zschau J (2009) Assessing building vulnerability using synergistically remote sensing and civil engineering. In: Kreck A, Rumor M, Zlatanova S, Fendel E (eds) *Urban and regional data management*. Taylor & Francis Group, London, pp 287–300
- Torres Y, Arranza JJ, Gaspar-Escribano JM, Haghia A, Martínez-Cuevasa S, Benitoa B, Ojedab JC (2019) Integration of LiDAR and multispectral images for rapid exposure and earthquake vulnerability estimation. Application in Lorca, Spain. *Int J Appl Earth Obs Geoinf* 81:161–175. <https://doi.org/10.1016/j.jag.2019.05.015>
- UN (2019) *World Population Prospects 2019: Highlights*. United Nations, Department of Economic and Social Affairs, Population Division. ST/ESA/SER.A/423
- UNISDR (2009) *Terminology on disaster risk reduction, united nations international strategy for disaster reduction; UNISDR-20-791 2009*. Switzerland, Geneva
- Villar-Vega M, Silva V, Crowley H, Yepes C, Tarque N, Acevedo A, Hube M, Coronel D, Santa Maria H (2017) Development of a fragility model for the residential building stock in South America. *Earthq Spectra* 33(2):581–604. <https://doi.org/10.1193/010716EQS005M>

- Wieland M, Pittore M (2016) Large-area settlement pattern recognition from Landsat-8 data. *ISPRS J Photogramm Remote Sens* 119:294–308. <https://doi.org/10.1016/j.isprsjprs.2016.06.010>
- Wieland M, Pittore M, Parolai S, Zschau J, Moldobekov B, Begaliev U (2012) Estimating building inventory for rapid seismic vulnerability assessment: towards an integrated approach based on multi-source imaging. *Soil Dyn Earthq Eng* 36:70–83. <https://doi.org/10.1016/j.soildyn.2012.01.003>
- Wu S-S, Qiu X, Wang L (2005) Population estimation methods in GIS and remote sensing: a review. *Gisci Remote Sens* 42(1):58–74. <https://doi.org/10.2747/1548-1603.42.1.80>
- Wyss M (2018) Rural Populations suffer most in great earthquakes. *Seismol Res Lett* 89(6):1991–1997. <https://doi.org/10.1785/0220180236>
- Wyss M, Speiser M (2022) Earthquake fatalities and potency. *Nat Hazards*
- Wyss M, Rosset P, Triveno L (2021) The ratio of rural/urban people killed in earthquakes needs to be assessed for countries separately, the example of Colombia. *Seismol Res Lett* 92(2A):1036–1051. <https://doi.org/10.1785/0220200252>
- Yepes-Estrada C, Silva V, Valcárcel J, Acevedo AB, Tarque N, Hube MA, Coronel G, Santa Maria H (2017) Modeling the residential building inventory in South America for seismic risk assessment. *Earthq Spectra* 33(1):299–322. <https://doi.org/10.1193/101915eqs155dp>

Publisher's Note Springer Nature remains neutral with regard to jurisdictional claims in published maps and institutional affiliations.

Authors and Affiliations

Christian Geiß¹  · Peter Priesmeier² · Patrick Aravena Pelizari¹ ·
 Angélica Rocio Soto Calderon³ · Elisabeth Schoepfer¹ · Torsten Riedlinger¹ ·
 Mabé Villar Vega⁴ · Hernán Santa María^{5,6} · Juan Camilo Gómez Zapata^{7,8} ·
 Massimiliano Pittore^{7,9} · Emily So¹⁰ · Alexander Fekete² · Hannes Taubenböck¹

¹ German Aerospace Center (DLR), German Remote Sensing Data Center (DFD), Weßling, Germany

² TH Köln – University of Applied Sciences, Cologne, Germany

³ Technical University of Munich, Munich, Germany

⁴ UME School, IUSS, Pavia, Italy

⁵ National Research Center for Integrated Natural Disaster Management (CIGIDEN), Santiago de Chile, Chile

⁶ Department of Structural and Geotechnical Engineering, Pontifical Catholic University of Chile, Santiago de Chile, Chile

⁷ Seismic Hazard and Risk Dynamics, GFZ German Research Centre for Geosciences, Potsdam, Germany

⁸ Institute for Geosciences, University of Potsdam, Potsdam, Germany

⁹ EURAC Research, Institute for Earth Observation, Bolzano, Italy

¹⁰ Centre for Risk in the Built Environment, University of Cambridge, Cambridge, UK